A finite volume model for maintaining stationarity and reducing spurious oscillations in simulations of sewer system filling and emptying

Arturo S. Leon, Zeda Yin & Abbas Sharifi

International Association
for Hydro-Environment
Engineering and Research

Hosted by
Spain Water and IWHR, China

Taylor & Francis
Taylor & Francis Group

Check for updates

RESEARCH PAPER

A finite volume model for maintaining stationarity and reducing spurious oscillations in simulations of sewer system filling and emptying

Arturo S. Leon, Zeda Yin and Abbas Sharifi

Department of Civil and Environmental Engineering, Florida International University, Miami, FL, USA

ABSTRACT

This paper introduces a model for simulating the unsteady dynamics of sewer systems filling and emptying, offering greater accuracy and stability. This article presents two novel contributions: first, the HLLS scheme (Harten–Lax–van Leer + Source term) is adapted to ensure the preservation of stationary conditions not only in free surface flows, as originally conceived, but also in pressurized flows and mixed flow scenarios. Second, a new method is proposed for the treatment of open channel flow cells near pressurization or adjacent to pressurized cells to minimize spurious oscillations when utilizing the two-component pressure approach (TPA) model. To verify the new model's effectiveness, it was tested for various conditions against the outcomes of the Open Source Field Operation and Manipulation (OpenFOAM) computational fluid dynamics (CFD) model. Furthermore, to demonstrate the model's potential for simulating real systems, the model was applied to three sewer systems that closely resemble real-world conditions, each of which had been intentionally modified for confidentiality purposes. The results show that the improved model successfully maintains stationary conditions within a sloped pipe across various flow conditions, while also preventing spurious oscillations at mixed flow interfaces even when using a pressure wave speed of $1000 \, \text{m s}^{-1}$.

1. Introduction

The design and operation of sewer systems (e.g. stormwater and combined) often requires simulating the filling and emptying of these systems, which involves complex flow dynamics including wetting/drying, open channel flows, pressurized flows, positive and negative mixed flow interfaces and stationary conditions. Free surface and pressurized flows are governed by different hyperbolic systems of equations making the simulation of mixed flows challenging compared to using a single governing equation (e.g. Aureli et al., 2015; Leon et al., 2009, 2010). Two main approaches unify the two governing equations in a single one to make the simulation more tractable. The first approach is the Preissmann slot model (PSM) that consists in adding an infinite slot to the cross-section (Cunge & Wegner, 1964). Kerger et al. (2011) proposed a negative slot to handle the problem of sub-atmospheric pressurized flows when using the Preismann method. The second method is the two-component pressure approach (TPA) model (Vasconcelos et al., 2006), which separates the total pressure into a hydrostatic pressure (open channel) and a surcharging pressure, the latter of which is calculated only in pressurized flow conditions (positive or negative pressure).

Several FV methods have been applied to transient open-channel, pressurized and mixed flows (e.g. Bourdarias & Gerbi, 2007; Capart et al., 1997; Leon et al., 2009, 2010; Sanders & Bradford, 2011). However, most of these approaches do not address 'lake at rest' or stationary conditions. These conditions become increasingly significant as pipe slope increases and may result in 'numerical storms' when flow velocity approaches zero. Numerical storms can manifest as non-physical oscillations in the water surface and relatively high flow velocities. In storm sewer systems, where consecutive rain events may occur within a short timeframe, parts of the system may experience near or at 'lake at rest' conditions. This includes sections of the pipe system fully submerged (pressurized flow), partially submerged (open channel flow), and areas where one side of the pipe is partially submerged while the other side is fully submerged (mixed flow). Therefore, preserving 'lake at rest' conditions is crucial in the context of open channel, pressurized and mixed flow scenarios.

Various numerical schemes were proposed for simulating mixed flows (e.g. Hodges, 2020; Kerger et al., 2011; Leon et al., 2009, 2010; Sanders & Bradford, 2011; Vasconcelos et al., 2006) when using two different hyperbolic systems of equations or a single

---

CONTACT Arturo S. Leon ✉ arleon@fiu.edu, artuleon@gmail.com

set of equations (PSM or TPA). Finite volume (FV) Godunov-type methods, in particular, were found to be well suited for solving hyperbolic systems of equations (e.g. shallow water equations) that involve discontinuities such as shocks (e.g. Guinot, 2000; Khani et al., 2021; Leon et al., 2009, 2010; Mao et al., 2020; Sanders & Bradford, 2011; Toro, 2001).

Spurious oscillations occur when using numerical schemes to simulate mixed flows within the Preissmann slot and TPA frameworks, even with relatively low pressure wave speeds (Aureli et al., 2015; Khani et al., 2021; Malekpour & Karney, 2016; Mao et al., 2020; Vasconcelos et al., 2009). These oscillations are especially evident when simulating filling bores (Aureli et al., 2015; Malekpour & Karney, 2016; Vasconcelos et al., 2009). Because the flow velocity during the filling of a pipe is at least two orders of magnitude lower than the velocities of acoustic waves in the pipe, the filling bore remains within a computational cell for multiple time steps (Malekpour & Karney, 2016; Vasconcelos et al., 2009). This extended duration is a result of the high magnitude of the acoustic wave velocity, which prompts the CFL stability criterion to impose a small computational time step (Malekpour & Karney, 2016; Vasconcelos et al., 2009). As the liquid depth within the computational cell being filled gradually increases, it generates a momentum imbalance on both sides of the filling bore, resulting in the creation of various types of waves in the pressurized flow region (Malekpour & Karney, 2016; Vasconcelos et al., 2009). These numerical oscillations become more pronounced with higher pressure wave speeds, and may compromise the results (e.g. Khani et al., 2021). Nonetheless, the resulting numerical oscillation is insignificant, except during the open channel-pressurized flow transition (Vasconcelos et al., 2009).

Various approaches were proposed to address the spurious oscillations. Vasconcelos et al. (2009) proposed numerical filtering and hybrid flux approaches, where numerical viscosity is increased by progressively raising wave velocities. They showed that these techniques control reasonably well the numerical oscillations for pressure wave speeds below about $100 \, \text{m s}^{-1}$. Malekpour and Karney (2016) proposed an approach that increases the numerical viscosity when the water level in a computational cell closely approaches the conduit roof and when the conduit's pressurization is imminent. Malekpour and Karney (2016) recommended increasing numerical viscosity in a distance of at least three times the height of the conduit. However, it was emphasized that under all circumstances, the number of cells subject to increased numerical viscosity should never be fewer than three. Mao et al. (2020) examined four oscillation-suppressing methods, including the one proposed by Vasconcelos et al. (2009), An et al. (2018), and Malekpour and Karney (2016), finding that only their proposed solver,

P_HLL, delivered satisfactory results at high acoustic wave speeds. The P_HLL increases the magnitude of the left and right wave speeds in the HLL Riemann solver when the flow depth exceeds a value between 70 to 90% of the conduit height (before pressurization). The magnitude increase of the wave speeds introduces numerical viscosity which is found to minimize spurious oscillations.

This paper is part of a long-term project which aims to develop a general physics-based machine learning model to predict sewer overflows and mitigate them through an optimal sequence of decision variables at control gates (e.g. schedule of partial or complete opening/closing of gates). The success of this project hinges on the ability of the model to handle the complex flow dynamics in sewer systems and to provide accurate solutions with least central processing unit (CPU) time. In particular, the model must accurately simulate stationary conditions, as the simulation period can extend over multiple storm events with dry intervals in between, during which the flow velocity in the system is zero, and the water stage in some pipes remains constant.

The present model was obtained after various trials by extracting the best characteristics of the various models proposed in the literature, in particular those proposed in the last decade. The resulting model was implemented in the existing open source Illinois Transient Model (ITM), which is a finite volume (FV) one-dimensional shock-capturing model that was originally made available in 2008 and since then was used for the design and operation of multiple sewer systems in the USA and worldwide. The major changes of ITM include: (1) replacing the two-governing equation model (Leon et al., 2010) of the original ITM with the two-component pressure approach model (Vasconcelos et al., 2006) to improve computational speed; (2) substituting the HLL Riemann solver with the HLLS scheme to maintain stationary conditions in sloped pipes not solely in free surface flows, as originally conceptualized (Franzini & Soares-Frazão, 2016; Murillo & García-Navarro, 2012), but also in pressurized flows and mixed flow scenarios; and (3) proposing a method to limit wave speeds in open channel flow cells near pressurization or adjacent to pressurized cells, aiming to minimize spurious oscillations when applying the TPA model to realistic pressure wave speeds (e.g. $\sim 1000 \, \text{m s}^{-1}$). This paper is divided as follows: first the governing equations are briefly described. Second, the numerical methods are presented along with the selection of wave speeds to minimize spurious oscillations in the transition from free surface to pressurized flow and vice versa. Third, the model is applied to three simple case studies, which are verified using CFD or laboratory measurements. Fourth, the model is applied to three sewer systems that closely resemble real-world conditions. The key results are summarized in the conclusions.

2. Governing equations and numerical model

The Saint-Venant equations for cross-sections of arbitrary shape can be written as Cunge et al. (1980), Capart et al. (2003), and Franzini and Soares-Frazão (2016):

$$\frac{\partial \mathbf{U}}{\partial t} + \frac{\partial \mathbf{F}}{\partial x} = \mathbf{S} \tag{1}$$

where the vector variable $\mathbf{U}$, the flux vector $\mathbf{F}$ and the source term vector $\mathbf{S}$ are given by:

$$\mathbf{U} = \begin{bmatrix} A \\ Q \end{bmatrix}, \quad \mathbf{F} = \begin{bmatrix} Q \\ \frac{Q^2}{A} + gI_1 \end{bmatrix} \quad \text{and}$$

$$\mathbf{S} = \begin{bmatrix} 0 \\ g\left[I_2 + A(S_o - S_f)\right] \end{bmatrix} \tag{2}$$

where A is the cross-sectional area of the flow; Q is flow discharge; g is gravitational acceleration, x is the longitudinal coordinate, t is time, S_o is the bed slope, and S_f is slope of the energy line. The term gI_1 represents the hydrostatic pressure thrust and is given by Capart et al. (2003):

$$gI_1 = g \int_0^h (h(x) - \eta)b(x, \eta)\, d\eta \tag{3}$$

where $h(x)$ is the flow depth, $b(x, \eta)$ is the channel width as a function of elevation (η) and along-stream location (x), and η is a local variable for the integration over the depth. Likewise, the term gI_2 represents the lateral pressure force due to the longitudinal width variation and is given by Capart et al. (2003):

$$gI_2 = g \int_0^h (h - \eta)\frac{\partial b(x, \eta)}{\partial x}\, d\eta \tag{4}$$

In Equation (4), it is observed that the term gI_2 is equal to zero for a prismatic channel. The variables gI_1 and gI_2 can be related as follows (e.g. Capart et al., 2003; Franzini & Soares-Frazão, 2016):

$$g\frac{\partial I_1}{\partial x} = gA\frac{\partial h}{\partial x} + gI_2 \tag{5}$$

As shown in Franzini and Soares-Frazão (2016), $g(I_2 + AS_o) = g[\partial I_1/\partial x - A\partial(h + z_b)/\partial x]$, where z_b is the bed elevation.

Similarly to the approach adopted by Leon et al. (2010), a reference state depth (h_{ref}) is established at the transition from open-channel to pressurized flow for circular conduits. This state is defined at an user-specified water depth (e.g. 95–99% of the maximum water depth in the cross-section). This reference state avoids having a zero top surface width, and hence an infinity gravity wave celerity.

For simulating pressurized flows, the two-component pressure approach (TPA) model (Vasconcelos et al., 2006) is adopted herein. In the TPA approach,

the term gI_1 in the momentum flux of Equation (2) is expressed as:

$$gI_1 = gA(h_c + h_s) \tag{6}$$

where h_c is the vertical distance between the free surface/pressurized flow threshold level (located h_{ref} above the pipe invert) and the centroid of the flow cross-sectional area, h_s is the surcharging pressure head which is calculated only in pressurized flow conditions (positive or negative pressure). In free surface flow conditions, h_s is set to zero. Because the pipe can expand or contract in the presence of positive or negative pressure heads, respectively, A is a function of the pressure head and pressure wave speed and can be calculated as follows:

$$A = A_{ref}\left(1 + \frac{gh_s}{a^2}\right) \tag{7}$$

where A_{ref} is the cross-sectional area of the flow corresponding to h_{ref} and a is the pressure wave speed. It is noted that a pressurized cell can depressurize at a ventilated location (e.g. manhole). In this case, the depressurized cell is switched back to open-channel flow, and h_s is set to 0. However, in non-ventilated locations, h_s could be negative, representing a negative pressure head in the pipe (Vasconcelos et al., 2006).

The governing equations are discretized using a first-order finite volume scheme and solved using an improved version of the well-known Harten–Lax–van Leer (HLL) approximate Riemann solver, which was initially introduced by Harten et al. (1983). In the HLL approach, the inclusion of source terms like friction is achieved through splitting methods and are not part of the Riemann solution (Toro, 2001). The improved solver used in this study is denoted as HLLS, following the nomenclature proposed by Murillo and García-Navarro (2012), wherein the first three letters (HLL) correspond to the HLL Riemann solver, and the fourth letter (S) indicates the incorporation of the source term as part of the Riemann solution. The HLLS Riemann solver was first introduced by Murillo and García-Navarro (2012) and later expanded by Franzini and Soares-Frazão (2016). The HLLS model is adopted for its easy handling of the source terms (e.g. all source terms are incorporated as part of the Riemann solution) and its ability to preserve stationary conditions. As shown in Figure 1, the HLLS model adds a stationary wave at $x = 0$ to represent the source terms. The stationary wave separates the middle region, also known as the star region ($\star$), into two regions, a left region (L) and a right region (R). According to this approach, the flow variables (A and Q) in cell i from the n to the $n + 1$ time level are updated as follows:

$$\mathbf{U}_i^{n+1} = \mathbf{U}_i^n + \frac{\Delta t}{\Delta x}(\mathbf{F}_{i-1/2}^R - \mathbf{F}_{i+1/2}^L) \tag{8}$$

where Δx is the length of the cell, Δt is the time step and the ith cell is centred at node i and extends from cell

interface $i - 1/2$ to $i + 1/2$. The flow variables $\mathbf{U}$ (A and Q) are defined at cell centres i and represent their average value within each cell. Fluxes, on the other hand, are evaluated at the interfaces between cells ($i - 1/2$ and $i + 1/2$). The fluxes in the HLLS Riemann solver are calculated as follows (Franzini & Soares-Frazão, 2016; Murillo & García-Navarro, 2012):

$$\mathbf{F}_{i+1/2}^{L}$$
$$= \begin{cases} \mathbf{F}_L & \text{if } 0 < S_L \\ \dfrac{\begin{array}{l} S_R\mathbf{F}_i - S_L\mathbf{F}_{i+1} \\ -S_RS_L(\mathbf{U}_i - \mathbf{U}_{i+1}) \\ +S_L(\mathbf{S}\Delta x - S_R\mathbf{H}) \end{array}}{S_R - S_L} & \text{if } S_L \leq 0 \leq S_R \\ \mathbf{F}_R - \mathbf{S}\Delta x & \text{if } 0 > S_R \end{cases} \quad (9)$$

$$\mathbf{F}_{i+1/2}^{R}$$
$$= \begin{cases} \mathbf{F}_L + \mathbf{S}\Delta x & \text{if } 0 < S_L \\ \dfrac{\begin{array}{l} S_R\mathbf{F}_i - S_L\mathbf{F}_{i+1} \\ -S_RS_L(\mathbf{U}_i - \mathbf{U}_{i+1}) \\ +S_R(\mathbf{S}\Delta x - S_L\mathbf{H}) \end{array}}{S_R - S_L} & \text{if } S_L \leq 0 \leq S_R \\ \mathbf{F}_R & \text{if } 0 > S_R \end{cases} \quad (10)$$

where $\mathbf{S}\Delta x$ is given by:

$$\mathbf{S}\Delta x = \begin{bmatrix} 0 \\ -g\overline{A}\delta(h + z_b) + g\delta I_1 - g\overline{AS_f}\Delta x \end{bmatrix} \quad (11)$$

where the overbar indicates averaged variables, as shown below. The symbol δ represents the spatial difference between the cell $i + 1$ and i. For instance, the term $g\delta I_1$ is given as follows:

$$g\delta I_1 = gA_{i+1}(h_{c\,i+1} + h_{s\,i+1}) - gA_i(h_{c\,i} + h_{s\,i}) \quad (12)$$

S_L and S_R in Equations (9) and (10) are the wave speed estimates for the left and right waves in Figure 1 and will be discussed below. In Equations (9) and (10), it is observed that the first and third fluxes represent supercritical flows, with the first moving to the right and the third moving to the left. On the other hand, the second flux in these equations corresponds to a subcritical flow, which can move either to the right or left. $\mathbf{H}$ in Equations (9) and (10) is a measure of the impact of the stationary wave associated to the source terms in the mass flux and is given by Murillo and García-Navarro (2012) and Franzini and Soares-Frazão (2016):

$$\mathbf{H} = \frac{-1}{S_RS_L} \begin{bmatrix} -g\overline{A}\delta(h + z_b) + \tilde{c}^2\delta A - g\overline{AS_f}\Delta x \\ 0 \end{bmatrix} \quad (13)$$

with

$$\overline{A} = \frac{A_i + A_{i+1}}{2}$$

$$\overline{S_f} = \tilde{u}|\tilde{u}|(n_M)_i(n_M)_{i+1}\left(\frac{P_i + P_{i+1}}{A_i + A_{i+1}}\right)^{4/3}$$

where n_M is the Manning's roughness coefficient, P is the wetted perimeter, $\tilde{u}$ is Roe's flow velocity and $\tilde{c}$ is
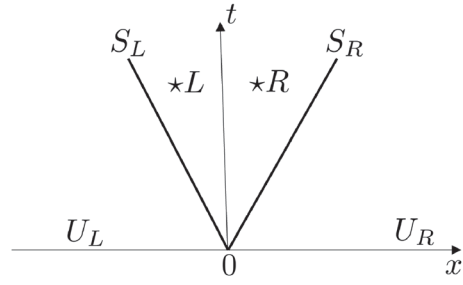

Figure 1. Principle of the HLLS Riemann solver in the phase space.

Roe's wave celerity. The expressions for $\tilde{u}$ and $\tilde{c}$ are as follows:

$$\tilde{u} = \frac{u_i\sqrt{A_i} + u_{i+1}\sqrt{A_{i+1}}}{\sqrt{A_i} + \sqrt{A_{i+1}}} \quad (14)$$

$$\tilde{c} = \sqrt{\frac{g}{2}\left(\frac{A_{i+1}}{T_{i+1}} + \frac{A_i}{T_i}\right)} \quad (15)$$

where T is the free surface width.

2.1. Maintaining stationary conditions in open channel, pressurized and mixed flow conditions

This section investigates the HLLS scheme to maintain stationary conditions not only in free surface flows, as originally conceptualized (Franzini & Soares-Frazão, 2016; Murillo & García-Navarro, 2012), but also in mixed and pressurized flows when using the TPA model.

In a mixed flow interface, the flow is open channel on one side of the interface and pressurized in the other side. The wave speed in the open channel region is in the order of 10 m s^{-1} while in the pressurized one is in the order of 1000 m s^{-1}. As is shown below, stationary conditions can be maintained by the HLLS scheme regardless of the flow regime as long as a single representative wave speed (c for open channel flows and a for pressurized flows) is used for each cell (e.g. cell i) and an averaged wave speed (e.g. $\tilde{c}$) is used at cell interfaces (e.g. $i - 1/2$).

Franzini and Soares-Frazão (2016) utilized Roe's wave speed estimates ($S_L = \tilde{u}_L - \tilde{c}_L$ and $S_R = \tilde{u}_R + \tilde{c}_R$) within the HLLS scheme, where the celerities $\tilde{c}_L$ and $\tilde{c}_R$ are defined for open channel flows only. Consistent with Franzini and Soares-Frazão (2016), we adopt Roe's estimates but modify the celerities to accommodate both open channel and pressurized flows as follows:

$$\tilde{c} = \sqrt{\frac{1}{2}(c_i^2 + c_{i+1}^2)} \quad (16)$$

where

$$c = \begin{cases} \sqrt{\frac{gA}{T}} & \text{for open channel flows} \\ a & \text{for pressurized flows} \end{cases} \quad (17)$$

where $\sqrt{gA/T}$ is the gravity wave speed and a is the pressure wave celerity. It is noted in Equation (16) that if the flows at both sides of the interface $(i + 1/2)$ are open channel, the Roe's estimate for $\tilde{c}$ is recovered (Franzini & Soares-Frazão, 2016). Subsequently, it will be shown that the HLLS approach is able to maintain stationary conditions regardless of the flow regime as long as an average celerity $(\tilde{c})$ is used at each cell interface. Following Equation (8), to update the variables A_i^n and Q_i^n at the next time step $(n + 1)$, we need to determine the fluxes at the cell interfaces ($\mathbf{F}_{i+1/2}^L$ and $\mathbf{F}_{i-1/2}^R$). For water at rest conditions, $z_{i-1} = z_i = z_{i+1}$, $u_{i-1} = u_i = u_{i+1} = 0$ and $Q_{i-1} = Q_i = Q_{i+1} = 0$. Substituting the respective values in Equations (9) and (10), the fluxes leaving and entering cell i ($\mathbf{F}_{i+1/2}^L$ and $\mathbf{F}_{i-1/2}^R$, respectively) are given by:

$$
\begin{aligned}
\mathbf{F}_{i+1/2}^L &= \frac{\tilde{c}}{2\tilde{c}}\begin{bmatrix} 0 \\ \boldsymbol{g}I_{1,i} \end{bmatrix} - \frac{-\tilde{c}}{2\tilde{c}}\begin{bmatrix} 0 \\ \boldsymbol{g}I_{1,i+1} \end{bmatrix} \\
&\quad - \frac{-\tilde{c}^2}{2\tilde{c}}\begin{bmatrix} A_i - A_{i+1} \\ 0 \end{bmatrix} + \frac{-\tilde{c}}{2\tilde{c}}\begin{bmatrix} 0 \\ \boldsymbol{g}\delta I_1 \end{bmatrix} \\
&\quad - \left(\frac{-\tilde{c}^2}{2\tilde{c}}\right)\left(\frac{-1}{-\tilde{c}^2}\right)\begin{bmatrix} \tilde{c}^2\delta A \\ 0 \end{bmatrix} \\
&= 0.5\begin{bmatrix} 0 \\ \boldsymbol{g}I_{1,i} \end{bmatrix} + 0.5\begin{bmatrix} 0 \\ \boldsymbol{g}I_{1,i+1} \end{bmatrix} \\
&\quad + \frac{\tilde{c}}{2}\begin{bmatrix} A_i - A_{i+1} \\ 0 \end{bmatrix} - 0.5\begin{bmatrix} 0 \\ \boldsymbol{g}\delta I_1 \end{bmatrix} \\
&\quad + \frac{1}{2\tilde{c}}\begin{bmatrix} \tilde{c}^2\delta A \\ 0 \end{bmatrix} \\
&= 0.5\begin{bmatrix} \tilde{c}(A_i - A_{i+1}) + \tilde{c}(A_{i+1} - A_i) \\ \boldsymbol{g}I_{1,i} + \boldsymbol{g}I_{1,i+1} - (\boldsymbol{g}I_{1,i+1} - \boldsymbol{g}I_{1,i}) \end{bmatrix} \\
&= \begin{bmatrix} 0 \\ \boldsymbol{g}I_{1,i} \end{bmatrix}
\end{aligned} \quad (18)
$$

$$
\begin{aligned}
\mathbf{F}_{i-1/2}^R &= \frac{\tilde{c}}{2\tilde{c}}\begin{bmatrix} 0 \\ \boldsymbol{g}I_{1,i-1} \end{bmatrix} - \frac{-\tilde{c}}{2\tilde{c}}\begin{bmatrix} 0 \\ \boldsymbol{g}I_{1,i} \end{bmatrix} \\
&\quad - \frac{-\tilde{c}^2}{2\tilde{c}}\begin{bmatrix} A_{i-1} - A_i \\ 0 \end{bmatrix} + \frac{\tilde{c}}{2\tilde{c}}\begin{bmatrix} 0 \\ \boldsymbol{g}\delta I_1 \end{bmatrix} \\
&\quad - \left(\frac{-\tilde{c}^2}{2\tilde{c}}\right)\left(\frac{-1}{-\tilde{c}^2}\right)\begin{bmatrix} \tilde{c}^2\delta A \\ 0 \end{bmatrix} \\
&= 0.5\begin{bmatrix} 0 \\ \boldsymbol{g}I_{1,i-1} \end{bmatrix} + 0.5\begin{bmatrix} 0 \\ \boldsymbol{g}I_{1,i} \end{bmatrix} \\
&\quad + \frac{\tilde{c}}{2}\begin{bmatrix} A_{i-1} - A_i \\ 0 \end{bmatrix} + 0.5\begin{bmatrix} 0 \\ \boldsymbol{g}\delta I_1 \end{bmatrix} \\
&\quad + \frac{1}{2\tilde{c}}\begin{bmatrix} \tilde{c}^2\delta A \\ 0 \end{bmatrix} \\
&= 0.5\begin{bmatrix} \tilde{c}(A_{i-1} - A_i) + \tilde{c}(A_i - A_{i-1}) \\ \boldsymbol{g}I_{1,i-1} + \boldsymbol{g}I_{1,i} + (\boldsymbol{g}I_{1,i} - \boldsymbol{g}I_{1,i-1}) \end{bmatrix} \\
&= \begin{bmatrix} 0 \\ \boldsymbol{g}I_{1,i} \end{bmatrix}
\end{aligned} \quad (19)
$$

It is noted from Equations (18) and (19) that for water at rest conditions, the fluxes leaving and entering cell i are the same regardless of the flow regime as long as an averaged celerity $(\tilde{c})$ is used at cell interfaces. For example, at cell interface $i + 1/2$, the averaged celerity will consider the celerities of cells i and $i + 1$ (Equation (16)).

2.2. Treatment of open channel flow cells near pressurization or adjacent to pressurized flows

In this study, we propose a simple approach to mitigate spurious oscillations that may occur when simulating mixed flows within the TPA framework. This approach is based on the observation that numerical viscosity can be controlled by changing the magnitude of the wave speed (e.g. LeVeque, 2002; Malekpour & Karney, 2016). For illustration purposes, similar to the approach in Malekpour and Karney (2016), we assume that the absolute magnitude of the left and right wave velocities (S_W) is the same $[S_L = -S_W$ and $S_R = S_W]$, and that the source terms are zero. With these assumptions, the fluxes in the intermediate region $(S_L \leq 0 \leq S_R)$ in Equations (9) and (10) are reduced to:

$$
F^\star = \frac{\mathbf{F}_i + \mathbf{F}_{i+1}}{2} - S_W\frac{(\mathbf{U}_{i+1} - \mathbf{U}_i)}{2} \quad (20)
$$

Equation (20) is identical to the one obtained by LeVeque (2002), among other authors. As demonstrated by LeVeque (2002), the first term on the right-hand side of Equation (20) results in an unconditionally unstable flux, necessitating stabilization through the influence of the second term, which introduces numerical viscosity into the scheme. As shown in Equation (20), the flux is minimized when the magnitude of the wave speed (S_W) is maximum. At the verge of pressurization, the gravity wave celerity c can be replaced with the pressure wave celerity to maximize numerical viscosity. The proposed approach exploits this characteristic.

The proposed approach consists of two steps. In the first step, for open channel flow cells that are on the verge of pressurization and exceed a certain water depth threshold (such as $h > h_{ref}$, where h_{ref} is a reference state depth slightly smaller than the pipe diameter that could range between 95% to 99% of pipe diameter), the gravity wave speed is set equal to the pressure wave celerity $(c = a)$. As an open channel cell approaches pressurization and its wave speed is adjusted to a, the magnitudes of the left and right wave speeds (S_L and S_R) undergo a large increase. Consequently, S_L and S_R attain large negative and positive values, respectively. This adjustment introduces numerical viscosity into the scheme.

In the second step, we check for cell interfaces with at least one surrounding cell (left or right) in free surface flow conditions. If, for such a cell, the intermediate

region (star region) as a solution of the Riemann problem gives a water depth larger than h_{ref}, the star region is assumed to be in pressurized flow conditions, and the fluxes calculated accordingly. The flow velocity and water depth in the star region are calculated using the rarefaction wave approximation (Leon et al., 2006):

$$u_\star = \frac{1}{2}(u_L + u_R) + \frac{1}{2}(\phi_L - \phi_R)$$
$$\phi_\star = \frac{1}{2}(\phi_L + \phi_R) + \frac{1}{2}(u_L - u_R)$$

(21)

where ϕ is calculated using the equation provided by Sanders and Bradford (2011) instead of the one given in Leon et al. (2006), owing to its explicit method of estimating the water depth from ϕ. The equation for ϕ from Sanders and Bradford (2011) is as follows:

$$\phi = 6.41 \sin(\theta/4)\sqrt{gd/8}$$

(22)

where θ is the wetted angle of a circular conduit. In Equation (22), it is noted that for a given ϕ, θ is explicitly determined, which, in turn, is used to calculate h, A, and c. If h is greater than h_{ref}, the flow in the star region is assumed to be pressurized, and hence the pressure wave celerity (a) is used. Otherwise, the flow is assumed to be in open channel conditions and is calculated according to Equation (17). The conditions in the star region (Equation (21)) are used to determine whether the flow in the cell interface will pressurize or not, considering the flow conditions in the left and right cells.

The original left and right wave speeds in the HLLS scheme use $S_L = \tilde{u} - \tilde{c}$ and $S_R = \tilde{u} + \tilde{c}$. These wave speeds may result in substantial numerical oscillations when the flow transitions from open channel to pressurized flow conditions. A better choice for the wave speeds that minimize spurious oscillations is as follows:

$$S_L = \min(u_L - c_L, \tilde{u} - \tilde{c}, u_\star - c_\star)$$
$$S_R = \max(u_R + c_R, \tilde{u} + \tilde{c}, u_\star + c_\star)$$

(23)

It is noted in Equation (23) that the goal is to increase the magnitude of the left and right wave speeds. In particular, the objective is to use the largest wave celerity resulting from either the flow in the cell (c_L or c_R), Roe's celerity ($\tilde{c}$), or that from the star region ($c_\star$). Even slightly better results in terms of minimizing spurious oscillations are obtained when $\tilde{c}$ that appears in Equation (13) is determined as:

$$\tilde{c} = \max(c_R, \tilde{c} \text{ (Equation (15))}, c_\star)$$

(1)

In all cases presented in this manuscript (test cases and actual systems), spurious oscillations were not substantial using the above considerations. It is worth mentioning that the proposed approach for minimizing spurious oscillations does not result in a substantial increase in computation time because pressurization is imminent. In such cases, the pressure wave speed (a) would be utilized regardless.

3. Computational fluid dynamics

The verification of the ITM results in this study was conducted using the Open Source Field Operation and Manipulation (OpenFOAM) model. OpenFOAM is an open source library that provides a range of C++ libraries and utilities for finite volume, finite element and Lagrangian particle tracking (Direct, 2017; Weller et al., 1998). Given the aim of simulating mixed flows that involve transient flows, the CompressibleInterFoam solver, which is integrated into OpenFOAM, is employed in all simulations. The CompressibleInterFoam solver uses the volume of fluid (VOF) method to simulate the interface between air and water. To generate the grid system for the three test cases, the OpenFoam utility polyDualMesh is utilized, following the approach described in Jasak et al. (2007) and Macpherson et al. (2009).

In all CFD simulations described in this study, the realizable k-epsilon turbulence model is employed. This choice is based on recommendations from several studies that have highlighted its suitability for simulating air–water interactions (e.g. Leon et al., 2019; Matveev, 2020). Moreover, the standard wall function, which is incorporated into the realizable k-epsilon model, can substantially enhance the accuracy of simulations at near-wall locations where the y^+ value is greater, as demonstrated in Boroomand and Mohammadi (2019). In this study, a y^+ value of 200 was employed to characterize the log-law layer.

Pressure–velocity coupling is achieved through the use of the PISO (Pressure Implicit with Splitting of Operators) algorithm in CompressibleInterFoam (Issa, 1986). The discretization of all spatial terms is performed using the second order upwind scheme, while the first order implicit scheme is used for temporal terms. To improve convergence, an adaptive time step is employed for all cases, and the maximum allowable global Courant number is set to 0.8.

To convert the Manning coefficient value into a sand-grain roughness height (to be used in the OpenFOAM simulations), three conversion equations [Equations (25) (USBR, 1997), (26) (Moody, 1947), (27) (Adams et al., 2012)] are utilized to obtain the sand-grain roughness values that can be used in OpenFOAM:

$$n_M = \sqrt{\frac{fR^{1/3}}{8g}}$$

(25)

$$f = \left[1.14 + 2\log_{10}\left(\frac{D}{\varepsilon}\right)\right]^{-2}$$

(26)

$$\varepsilon = 11.03k$$

(27)

where f is the Darcy–Weisbach friction factor, R is the hydraulic radius, ε is average height of surface irregularities, D is pipe diameter, and k is the sand-grain roughness height.

To account for the compressibility of air, the ideal gas law is employed, with an operational density of $1.225 \, \text{kg m}^{-3}$. The speed of sound is converted to isotropic bulk modulus using Equation (28):

$$K_s = \rho a^2 \tag{28}$$

where K_s is the isotropic bulk modulus, and a is the sound speed in water, which is the same as the pressure wave speed. As pointed out by Mandair et al. (2020), the pressure wave speed is influenced by pipe wall deformation. However, our CFD model disregards fluid–structure interaction and maintains a constant cross-sectional area. Consequently, this compressibility model is only partially physical, as the depiction of pipe elastic effects is approximated by the wave speed.

4. Numerical tests

The objective of this section is to evaluate the accuracy of the proposed model using three simple but representative test cases. The first test case objective was to showcase the ability of the model in achieving stationarity in all flow regimes (open channel flows, pressurized flows and mixed flow interfaces). The second test case objective was to demonstrate the capability of the model in simulating a positive mixed flow interface for a realistic pressure wave celerity without producing significant numerical oscillations. The third test case objective was to demonstrate the capability of the model to simulate full pipe flows with negative gauge pressures using the experiments reported in Vasconcelos et al. (2006). For the Open-FOAM meshing, prior to the conversion to a polyhedral mesh, a tetrahedral mesh was generated with target sizes of 0.05, 0.05 and 0.01 m for cases 1, 2 and 3, respectively. The target size is the same for test cases 1 and 2, attributed to their similar geometric scale (e.g. pipe diameter). In contrast, the third test case has a smaller target size, reflective of the reduced scale of the setup itself. The results of the ITM model are compared with those of the Open-FOAM model, as well as laboratory data wherever possible.

4.1. Test 1: flow stationarity

The aim of this test is to showcase the ability of the proposed model in achieving stationarity in all flow regimes (open channel flows, pressurized flows and mixed flow interfaces) and for a relatively large slope pipe system (10%). The test case is designed in such a way that the pipe system has all the above flow regimes and the ITM screenshot of the initial flow conditions is illustrated in Figure 2. The system consists of two pipes, with the left pipe having a 10% downward slope (positive slope) and the right pipe exhibiting a 10% upward slope (negative slope). Both pipes have a length of 50 m, a diameter of 3 m, a Manning's roughness coefficient of 0.013, and a pressure wave celerity of $1000 \, \text{m s}^{-1}$.

The initial water elevation in the entire system is set to 54 m. The simulation was performed using 2000 cells in each conduit and a Courant number of 0.80. In the ITM model, a uniform time step is applied across the entire pipe domain.

The CFD results for water elevation and velocity indicate a simulation precision of 2×10^{-3} and 8×10^{-7}, respectively. It is evident from these findings that the CFD model struggle to maintain stationarity conditions. Conversely, ITM demonstrates the ability to sustain stationarity conditions for both water elevation and velocity, approaching the precision limit of double-precision computation (accuracy up to fifteen decimal places).

4.2. Test 2: positive mixed flow interface

The purpose of this test is to demonstrate the capability of the proposed model in simulating a positive mixed flow interface for a realistic pressure wave celerity without producing significant numerical oscillations. The test configuration, as shown in Figure 3, consists of two pipes, with the left pipe having a 2% downward slope (positive slope) and the right pipe exhibiting a 2% upward slope (negative slope). Both pipes have a length of 20 m, a diameter of 0.5 m, a Manning's roughness coefficient of 0.015, and a pressure wave celerity of $1000 \, \text{m s}^{-1}$. The initial flow in both pipes is set at $0.15 \, \text{m}^3 \, \text{s}^{-1}$, with a normal depth of 0.1958 m and a Froude number of 1.76 (supercritical flow). The collision of these opposing flows in the supercritical regime at the intersection of the pipes generates two hydraulic bores. Initially, these bores exhibit open channel flow conditions, eventually transitioning to pressurized conditions, forming a mixed flow interface. The upstream and downstream boundary conditions (BC) are set to be equal to the initial discharge in the pipe with a flow depth equal to the normal depth ($Q_{BC} = 0.15 \, \text{m}^3 \, \text{s}^{-1}$ and $h_{BC} = 0.1958 \, \text{m}$). The simulation was performed using 4000 cells in each conduit and a Courant number of 0.80. The time for outputting the results is 0.0001 s.

Figures 4 and 5 illustrate the pressure head and average velocity time traces at point 1 (situated at midway of the left pipe) for both the ITM and CFD models. For complementing the ITM results, Figure 6 presents the piezometric head at three time snapshots (2, 6 and 10 s). The simulation was limited to 10 s due to the extensive CPU time required for the CFD model with a pressure wave celerity of $1000 \, \text{m s}^{-1}$, which amounted to approximately three weeks. As shown in Figures 4 and 5, the ITM and CFD models exhibit a good agreement for both the pressure head and velocity. As depicted in Figure 4, the CFD model, simulating air–water flows, reveals small fluctuations in the pressure head before the positive interface arrives P1, indicative of slight surface instabilities. Surface instabilities are known to
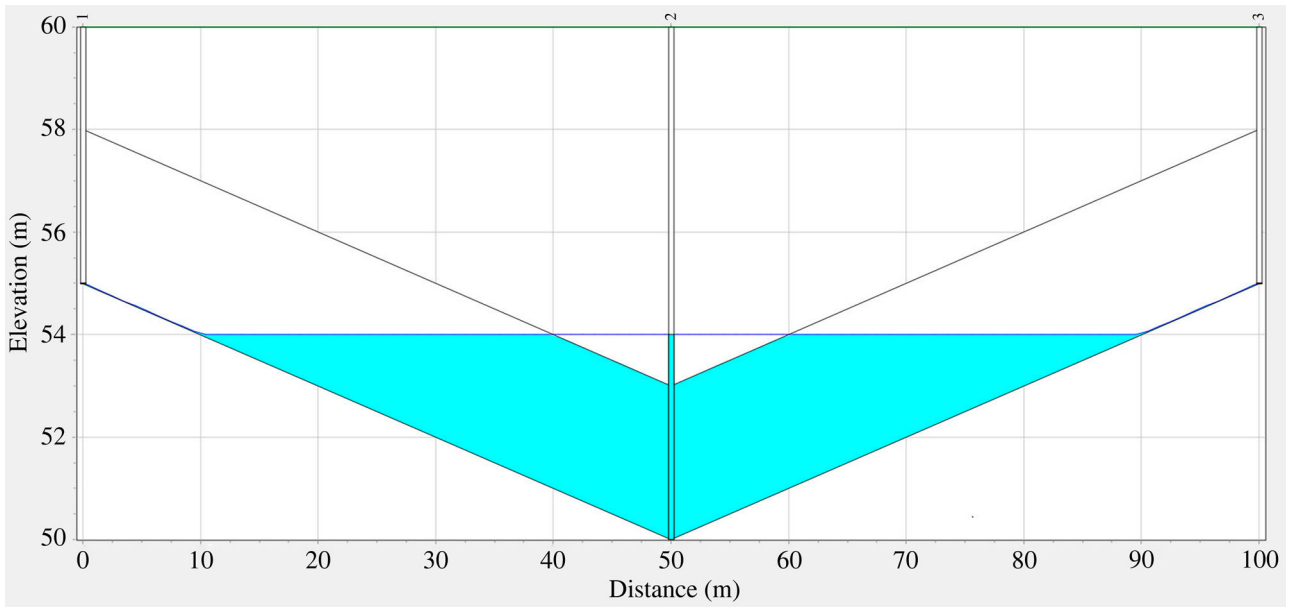
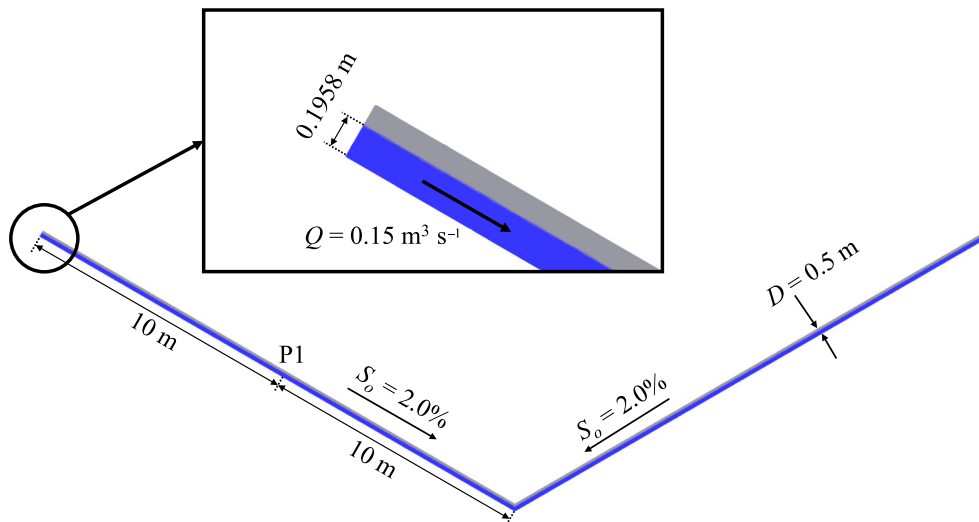**Figure 2.** Geometry of Test 1 showing the initial water elevation.

Figure 3. Geometry configuration for Test 2.

occur in supercritical flows due to pronounced interactions between air and water (Kramer & Chanson, 2018). ITM lacks the capability to simulate surface instabilities because it is a single-phase model. Consequently, as depicted in Figure 4, the pressure head in the ITM model remains constant until the positive interface reaches P1.

After the positive interface arrives at P1, as shown in Figure 4, the CFD model depicts a constant hydraulic jump in open channel conditions for about one second (8.2 to 9.3 s) before fully pressurizing. The ITM model also predicts a hydraulic jump in open channel conditions before fully pressurizing; however, the hydraulic jump depth in the ITM model is slightly overpredicted. After pressurization, the pressure head

in both models is more or less the same. Figure 4 also shows that the maximum pressure fluctuations in the ITM model during pressurization is small (~ 2 cm) even when the pressure wave celerity used in the simulations is 1000 m s^{-1}. It is worth noting that these small oscillations, with a frequency corresponding to that of the acoustic wave, remain imperceptible in the piezometric head plot (Figure 6). They originate from the propagation of acoustic waves within the pressurized section of the pipe. The results for the average velocity (Figure 5) exhibit a good agreement between both models, particularly regarding the timing of the positive interface arrival and the velocity magnitude after the positive interface reaches P1.
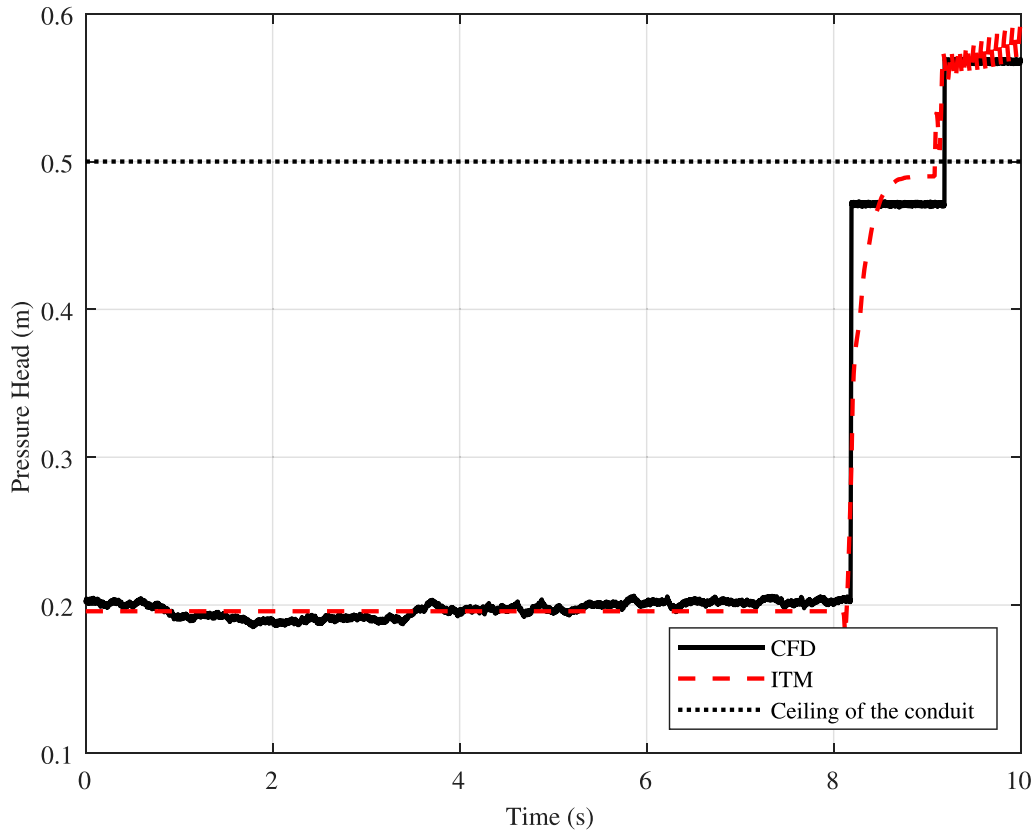
Figure 4. Test 2: pressure head (m) time trace at P1 for the CFD and ITM models.
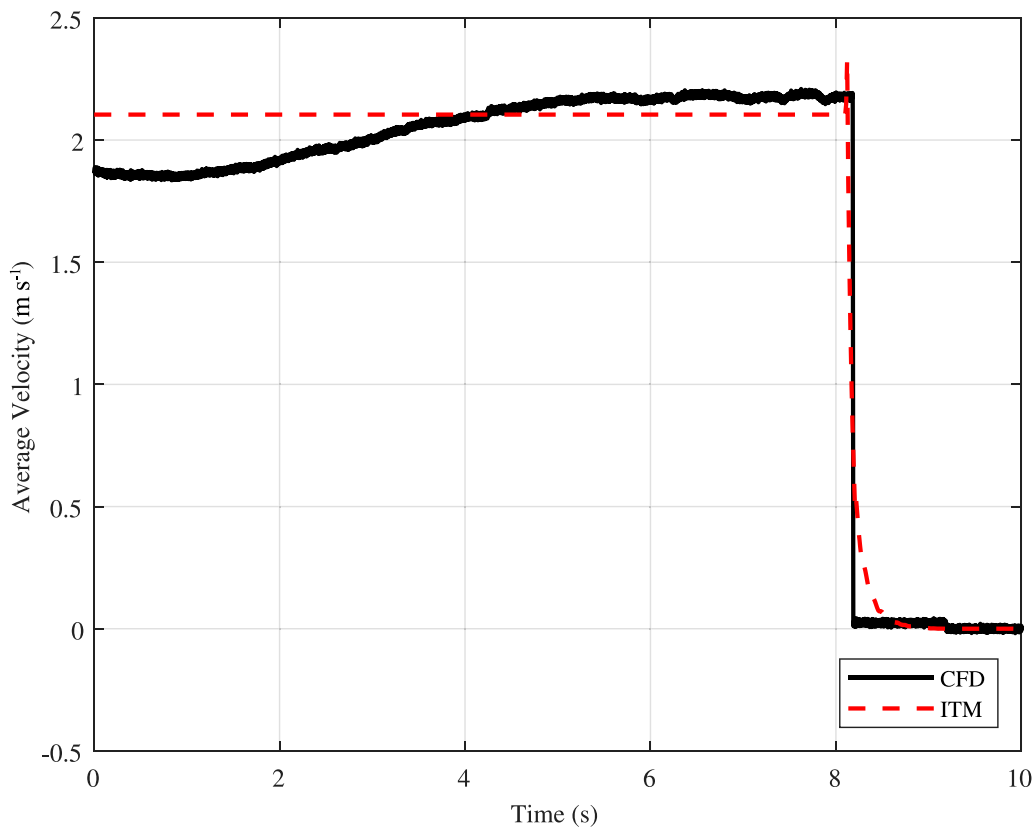

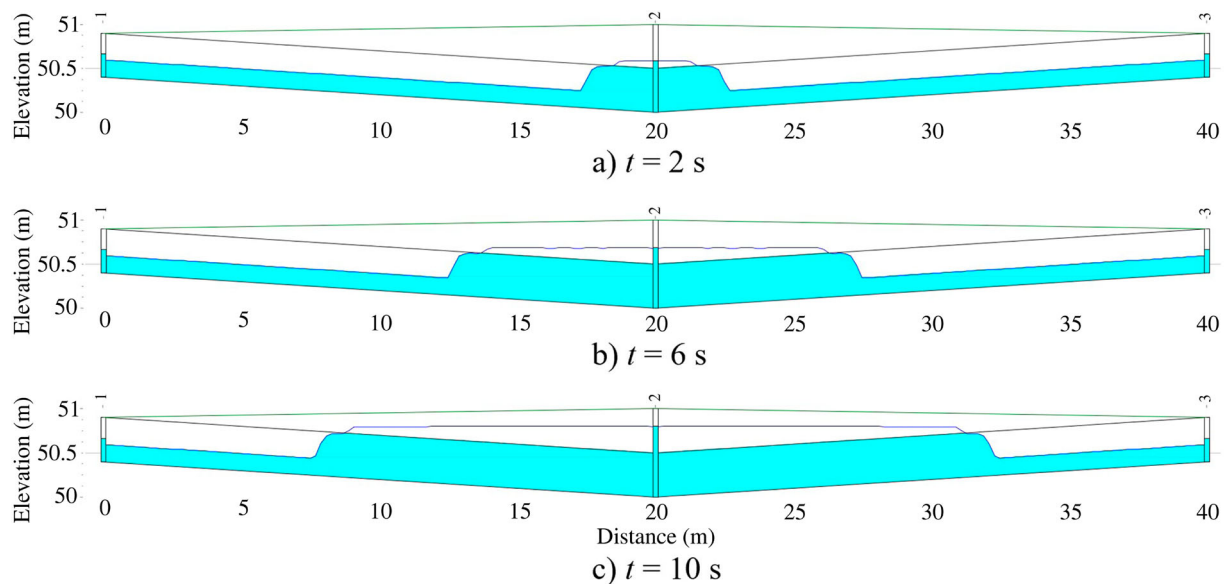**Figure 5.** Test 2: average velocity (m s^{-1}) time trace at P1 for the CFD and ITM models.

Figure 6. Test 2: ITM piezometric head for Test case 2 at three different time snapshots.

4.3. Test 3: negative piezometric pressure flows

This test demonstrates the capability of the proposed model to simulate full pipe flows with negative gauge pressures using the experiments reported in Vasconcelos et al. (2006), the laboratory setup for which is shown in Figure 7. To create conditions where negative pressure heads would emerge, the centre portion of the pipeline was elevated. The first half of the pipe had an upward slope of roughly 2.0%, while the second half had a corresponding downward slope, with the pipe being elevated approximately 0.15 m at the centre compared to the ends. The experimental setup is comprised of an acrylic pipeline with an inner diameter of 9.4 cm and a length of 14.33 m, connected at its upstream end by a box tank and at its downstream end by a cylindrical tank. The pressure wave celerity used in the simulations was $300\,\mathrm{m\,s^{-1}}$; this value was obtained from experimental measurements of pressure pulse propagation between two pressure transducers, as reported in Vasconcelos et al. (2006). Simulations of the ITM model were conducted using 400 cells and a Courant number (Cr) value of 0.80. The outflow was assumed constant and a value of $0.45\,\mathrm{1\,s^{-1}}$ was estimated by observing the change in water volume over time. For estimating energy losses, Vasconcelos et al. (2006) used a Manning roughness coefficient of 0.012, which was also used in this test case. The meshing used in the CFD simulation is presented at the beginning of the numerical tests section, while the methodology used in the simulations is described in the computational fluid dynamics section.

The system was filled to a level of 0.30 m at the box tank, and after achieving stationary conditions, a syphon outflow was abruptly initiated at the box tank at $t = 0$. As the water level in the box tank decreased, sub-atmospheric pressures were created at the centre of the pipe, resulting in a complex flow pattern. When the water level at the box tank fell below the pipe crown, air at atmospheric pressure from the box tank interacts with the sub-atmospheric pressure in the pipe resulting in a complex two-phase flow phenomena. Because the ITM model is unable to simulate two-phase flows, the comparison between the model predictions and experimental results is presented until right before the air intrusion from the box tank into the pipe. In the experiment, this air intrusion occurred at $t = 42.5\,\mathrm{s}$ (Vasconcelos et al., 2006), while in the ITM model, it occurred approximately one second earlier ($t \approx 41.5\,\mathrm{s}$).

Figure 8 shows the experimental and simulated velocities at a distance of 9.9 m downstream of the box tank for both CFD and ITM models. Meanwhile, Figure 9 illustrates the experimental and model predictions of piezometric depth at 14.1 m downstream of the box tank. As demonstrated in these figures, the ITM and CFD models show satisfactory agreement with the experimental data for both velocity and pressure head. The velocity results from both models match the experimental data well in terms of the frequency of oscillations, but overestimate the velocity amplitudes. As suggested by Vasconcelos et al. (2006), this could be due, in part, to the assumption of uniform outflow being inaccurate, and the neglect of minor losses and unsteady friction in the model. It is worth noting that the ITM model and most one-dimensional sewer models consider only steady friction factors (e.g. Manning's equation), which are known to underestimate the rate of attenuation of the pressure and velocity oscillations (e.g. Tosan et al., 2022; Zhou et al., 2019).

5. Application to three actual sewer systems

This section presents the ITM input files and videos with the corresponding simulation results for three sewer systems that closely resemble real-world conditions.
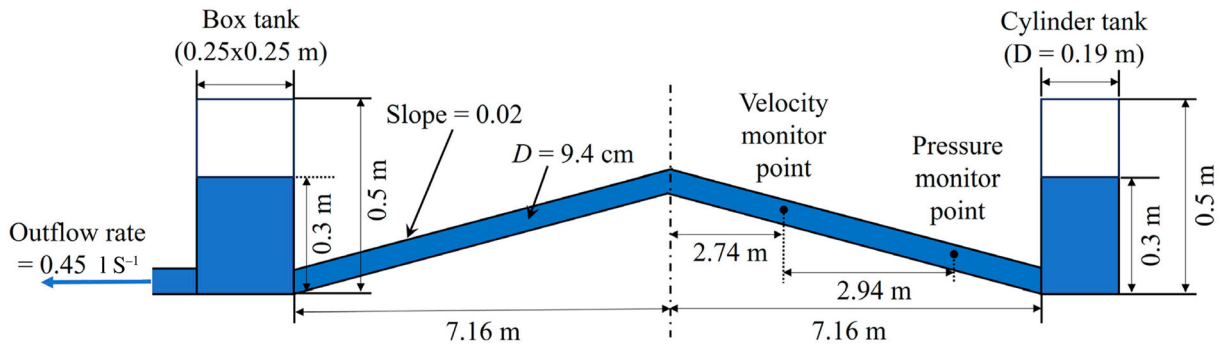
Figure 7. Geometry of Test 3. This test case corresponds to the experiment in Vasconcelos et al. (2006).
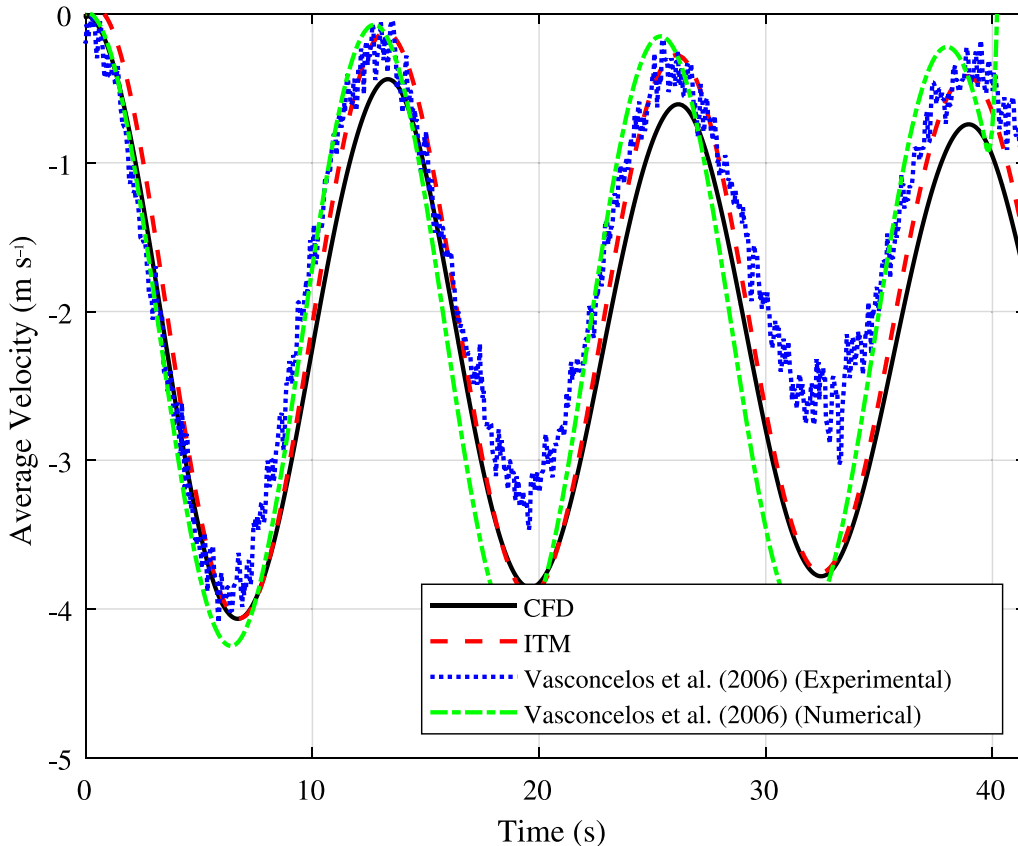

Figure 8. Test 3: simulated and measured average velocity (m s^{-1}) time trace in study point P2.

The three sewer systems are denoted as cases A, B and C. A brief description of these sewer systems along with the links for the input files and corresponding videos are presented below. The three input files and accompanying videos showcasing the results are available on GitHub at the following link: https://github.com/artuleon/ITM_version2_0/blob/main/README.md.

5.1. Case A

This sewer system encompasses a complex sewer network involving the operation of three pumps depending on the water depth at control nodes. The system includes a three-way junction, dropshafts and reservoirs, as shown in Figure 10. Besides GitHub, the input file can be obtained from the following link: https://web.eng.fiu.edu/arleon/ITM/InputFiles/CASEA.inp. To

illustrate a close-up view of tunnel pressurization and depressurization, the reader can find the video depicting the pressure head results between nodes *DAC1* and *03* at the following link: https://web.eng.fiu.edu/arleon/ITM/Videos/ITM_CASEA.mp4.

As can be observed in the video, the system begins in a dry state and subsequently switches to free surface flow conditions as inflows enter the system. When the control nodes reach thresholds pre-defined in a control curve, the pumps begin to operate. The video shows that dropshafts *DAC1*, *07*, *06* and *05*, along with a section of the tunnel system surrounding these nodes, experience pressurization due to significant inflows without exhibiting apparent numerical instabilities. Eventually, as the inflows subside, the pressurized regions depressurize and return to open-channel flow conditions without displaying any apparent numerical
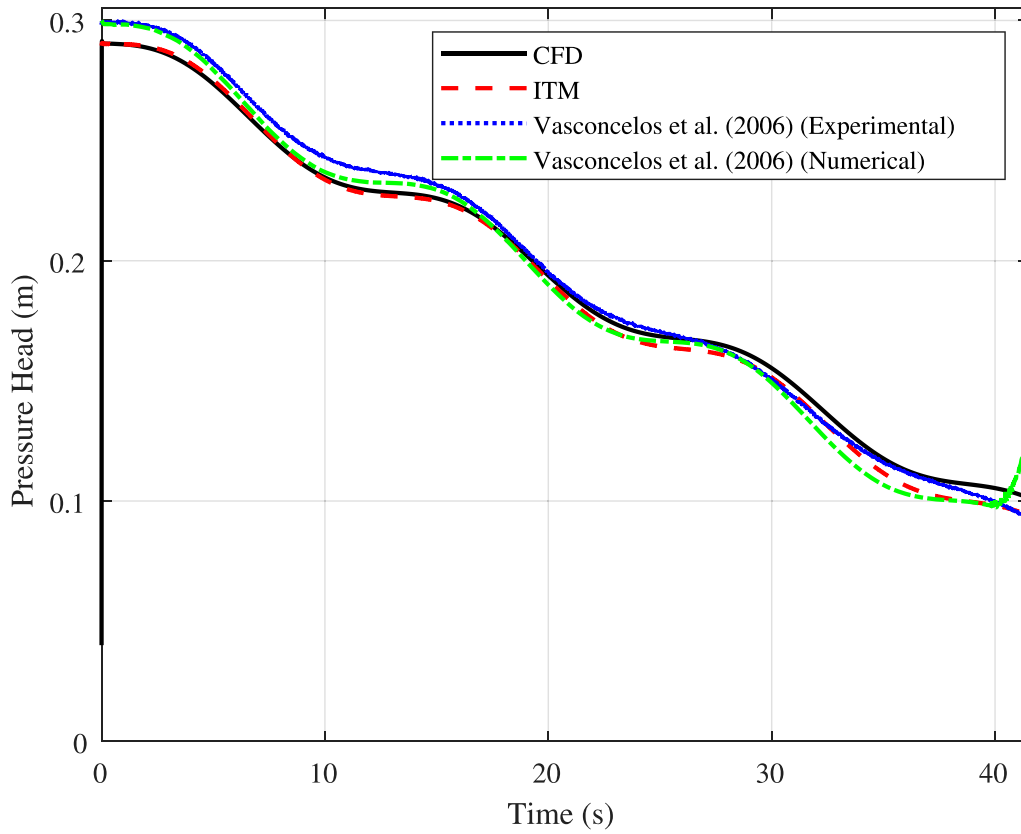
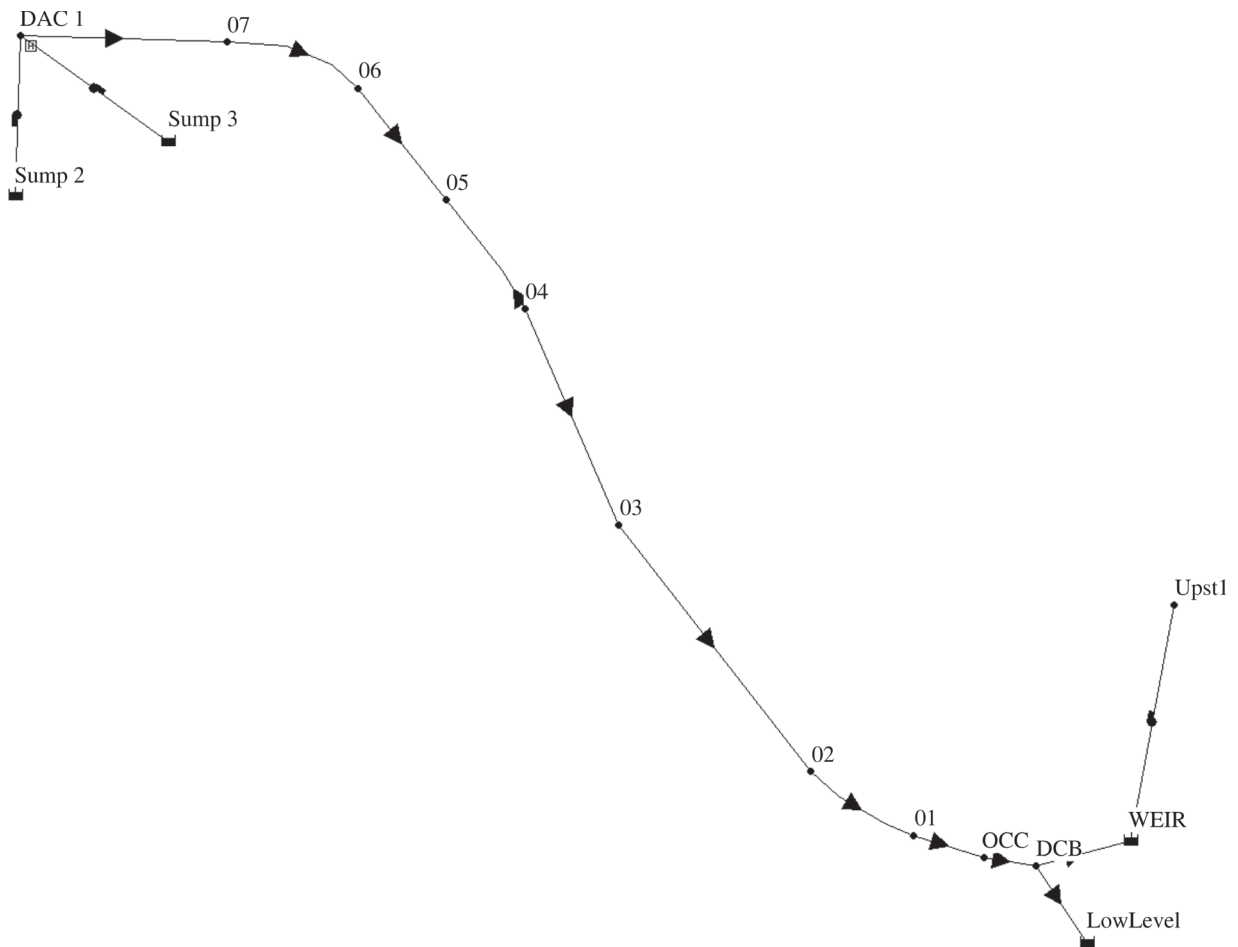**Figure 9.** Test 3: simulated and measured pressure head (m) time trace in study point P1.

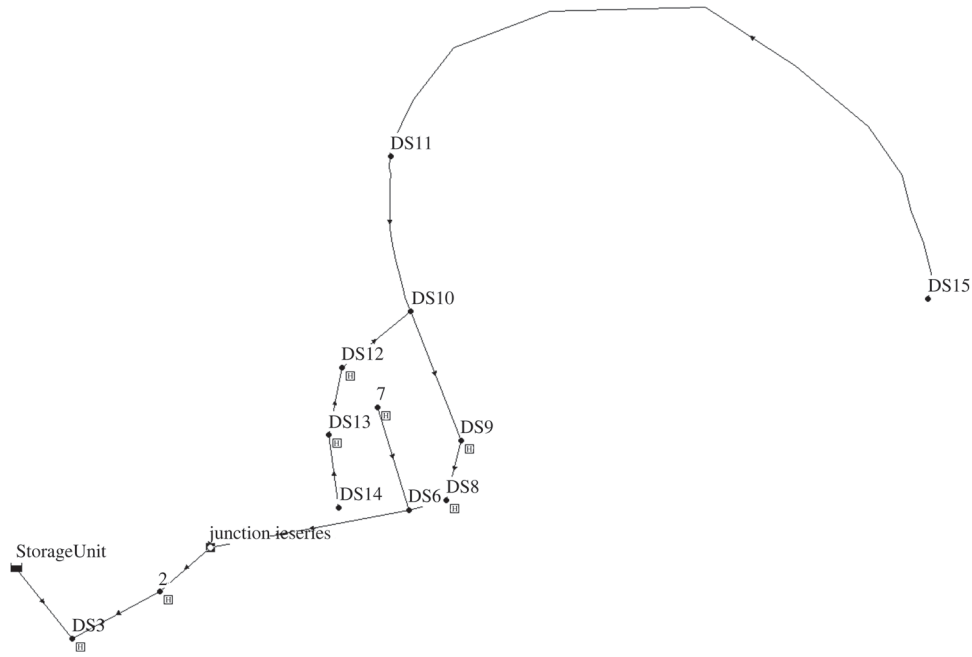**Figure 10.** Schematic of sewer system for Case A.

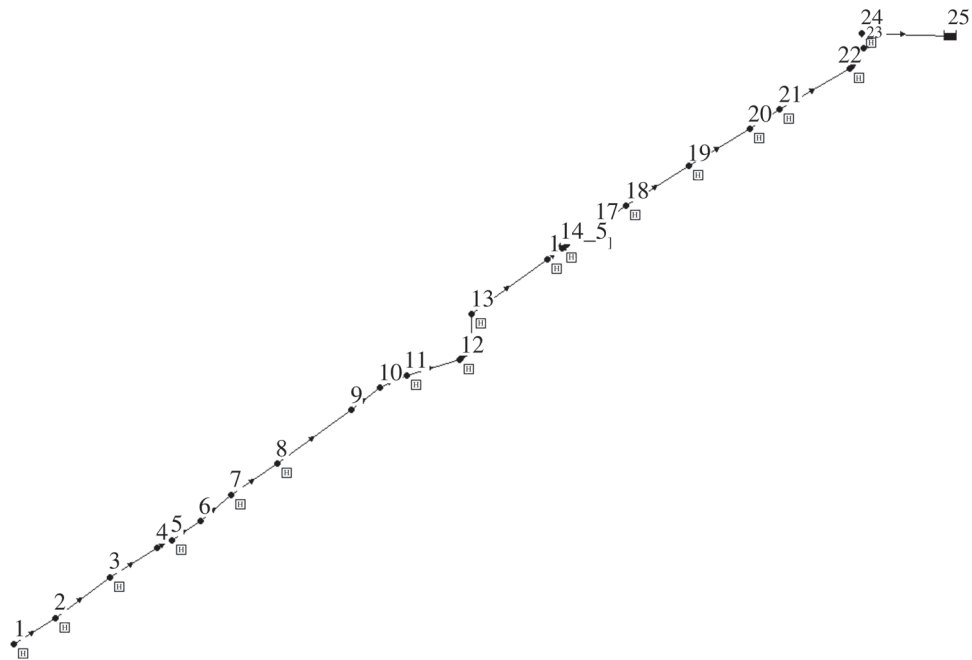**Figure 11.** Schematic of sewer system for Case B.

Figure 12. Schematic of sewer system for Case C.

instabilities. As pumping continues, most of the piping system transitions to a dry state.

5.2. Case B

This sewer system encompasses a complex sewer network involving two gates, one of which is operated according to the specified time of the simulation (time series) and the second, depending on the water depth at a control node. The system includes three-way junctions, multiple dropshafts with inflow hydrographs and a weir, as shown in Figure 11. Besides GitHub, the input file can be obtained from the following link: https://

web.eng.fiu.edu/arleon/ITM/InputFiles/CASEB.inp. The video of the pressure head results between nodes *DS3* and *DS12* can be obtained from the following link: https://web.eng.fiu.edu/arleon/ITM/Videos/ITM_CAS EB.mp4.

The operation of the gates, coupled with significant inflow hydrographs, causes the pressurization of various parts of the system. The video shows the upstream propagation of a mixed flow interface passing various dropshafts with inflow hydrographs without exhibiting substantial numerical instabilities. It is noted that some oscillations are evident when the positive mixed flow interface passes through dropshafts with inflows. The

inflows add mass to the system, creating oscillations, especially when the flow is pressurized.

5.3. Case C

This sewer system encompasses a sewer network involving multiple dropshafts with inflow hydrographs, as shown in Figure 12. Besides GitHub, the input file can be obtained from the following link: https://web.eng.fiu.edu/arleon/ITM/InputFiles/CASEC.inp.   The video of the pressure head results between nodes 1 and 11 can be obtained from the following link: https://web.eng.fiu.edu/arleon/ITM/Videos/ITM_CASEC.mp4.

As can be observed in the video, a mixed flow interface propagates upstream passing various dropshafts with inflow hydrographs without exhibiting substantial numerical instabilities. In a similar way to Case B, some oscillations are evident when the positive mixed flow interface passes through dropshafts with inflows.

6. Conclusions

The present paper presents an improved shock-capturing finite volume one-dimensional model, which was implemented in the existing open source Illinois Transient Model (ITM). The major changes made to ITM include replacing the original two-governing equation model with the two-component pressure approach model to improve computational speed, using an improved Riemann solver that preserves stationary conditions in sloped pipes, and proposing a new method for the treatment of open channel flow cells near pressurization or adjacent to pressurized cells to minimize spurious oscillations when utilizing the TPA model. The accuracy of the new ITM model was tested using three test cases. The model's performance was compared with those of a commonly used computational fluid dynamics (CFD) model. Moreover, to demonstrate the model's potential for simulating real systems, the model was applied to three sewer systems that closely resemble real-world conditions. The key results are as follows:

(1) The results indicate that the ITM model is capable of achieving 'lake at rest' conditions (horizontal still water) for steep slopes, when the flow is adjacent to dry regions (wet-dry bed interfaces), and under partial open-channel and partial surcharged flow conditions. No ITM simulations displayed the characteristics of 'numerical storms'.

(2) The results demonstrate that the ITM model can simulate positive mixed flow interfaces without generating significant numerical oscillations even when using a pressure wave speed of $1000 \, \mathrm{m \, s^{-1}}$.

(3) Although the ITM simulations for the three intentionally modified sewer systems were not verified using CFD due to the systems' large scale, the videos of the simulations show qualitatively reasonable results.

Disclosure statement

No potential conflict of interest was reported by the author(s).

Notation

A	cross-sectional area of the flow (m^2)
a	pressure wave speed (m s^{-1})
A_{ref}	cross-sectional area of the flow corresponding to h_{ref} (m^2)
b	channel width as a function of elevation (η) and along-stream location (x) (m)
D	pipe diameter (m)
$\mathbf{F}$	flux vector (m^3 s^{-1} or m^4 s^{-2})
f	Darcy–Weisbach friction factor (−)
$\mathbf{g}$	gravitational acceleration (m s^{-2})
$\mathbf{g}I_1$	represents hydrostatic pressure thrust (m^4 s^{-2})
$\mathbf{g}I_2$	represents lateral pressure force due to longitudinal width variation (m^3 s^{-2})
$\mathbf{H}$	measure of the impact of the stationary wave associated to the source terms in the mass flux (first and second row of vector, respectively) (m^2 s^{-1}; m^3 s^{-2})
h	flow depth (m)
h_c	distance between the free surface and the centroid of the flow cross-sectional area (m)
h_{ref}	reference state depth (m)
h_s	surcharging pressure head (m)
k	sand-grain roughness height (m)
n_M	Manning's roughness coefficient (−)
P	wetted perimeter (m)
Q	flow discharge (m^3 s^{-1})
R	hydraulic radius (m)
$\mathbf{S}$	source term vector (first and second row of vector, respectively) (m^2 s^{-1}; m^3 s^{-2})
S_f	energy line slope (−)
S_L, S_R	left and right wave speed, respectively (m s^{-1})
S_o	bed slope (−)
T	free surface width (m)
t	time (s)
$\mathbf{U}$	vector variable (first and second row of vector, respectively) (m^2 s^{-1}; m^3 s^{-2})
u	flow velocity (m s^{-1})
x	longitudinal coordinate (m)
δ	spatial difference between cell $i+1$ and i (−)
ε	average height of surface irregularities (m)
ϕ	variable that is a function of the water depth and that is needed to calculate $u_\star$ (m s^{-1})
η	local variable for integration over the depth (m)

Data availability statement

All data and code that support the findings of this study are available from the corresponding author. The ITM model can be found at the website of the Illinois Transient Model (https://web.eng.fiu.edu/arleon/ITM.htm). The input files for the three actual sewer systems can be found at https://web.eng.fiu.edu/arleon/ITM/InputFiles/CASEA.inp, (https://web.eng.fiu.edu/arleon/ITM/InputFiles/CASEB.inp), and (https://web.eng.fiu.edu/arleon/ITM/InputFiles/CASEC.inp).

References

Adams, T., Grant, C., & Watson, H. (2012). A simple algorithm to relate measured surface roughness to equivalent sand-grain roughness. *International Journal of Mechanical Engineering and Mechatronics*, *1*(2), 66–71.

An, H., Lee, S., Noh, S. J., Kim, Y., & Noh, J. (2018). Hybrid numerical scheme of Preissmann slot model for transient mixed flows. *Water*, *10*(7), 899. https://doi.org/10.3390/w10070899

Aureli, F., Dazzi, S., Maranzoni, A., & Mignosa, P. (2015). Validation of single- and two-equation models for transient mixed flows: A laboratory test case. *Journal of Hydraulic Research*, *53*(4), 440–451. https://doi.org/10.1080/00221686.2015.1038324

Boroomand, M. R., & Mohammadi, A. (2019). Investigation of k-ε turbulent models and their effects on offset jet flow simulation. *Civil Engineering Journal*, *5*(1), 127. https://doi.org/10.28991/cej-2019-03091231

Bourdarias, C., & Gerbi, S. (2007). A finite volume scheme for a model coupling free surface and pressurised flows in pipes. *Journal of Computational and Applied Mathematics*, *209*, 109–131. https://doi.org/10.1016/j.cam.2006.10.086

Capart, H., Eldho, T. I., Huang, S. Y., D. L. Young, & Zech, Y. (2003). Treatment of natural geometry in finite volume river flow computations. *Journal of Hydraulic Engineering*, *129*(5), 385–393. https://doi.org/10.1061/(ASCE)0733-9429(2003)129:5(385)

Capart, H., Sillen, X., & Zech, Y. (1997). Numerical and experimental water transients in sewer pipes. *Journal of Hydraulic Research*, *35*, 659–672. https://doi.org/10.1080/00221689709498400

Cunge, J. A., Holly, F. M., & Verwey, A. (1980). *Practical aspects of computational river hydraulics*. Pitman Publ. Inc.

Cunge, J. A., & Wegner, M. (1964). Numerical integration of barré de saint-venant's flow equations by means of an implicit scheme of finite differences. applicants in the case of alternately free and pressurised flow in a tunnel. *La Houille Blanche*, *50*(1), 33–39. https://doi.org/10.1051/lhb/1964002

Direct, C. (2017). Openfoam 5.0. *The OpenFOAM Foundation Ltd*.

Franzini, F., & Soares-Frazão, S. (2016). Efficiency and accuracy of lateralized hll, hlls and augmented roe's scheme with energy balance for river flows in irregular channels. *Applied Mathematical Modelling*, *40*(17), 7427–7446. https://doi.org/10.1016/j.apm.2016.02.007

Guinot, V. (2000). Riemann solvers for water hammer simulations by godunov method. *International Journal for Numerical Methods in Engineering*, *49*(7), 851–870. https://doi.org/10.1002/1097-0207(20001110)49:7<1.0.CO;2-S

Harten, A., Lax, P. D., & Leer, B. V. (1983). On upstream differencing and godunov-type schemes for hyperbolic conservation laws. *SIAM Review*, *25*(1), 35–61. https://doi.org/10.1137/1025002

Hodges, B. R. (2020). An artificial compressibility method for 1D simulation of open-channel and pressurized-pipe flow. *Water*, *12*(6), 1727. https://doi.org/10.3390/w12061727

Issa, R. I. (1986). Solution of the implicitly discretised fluid flow equations by operator-splitting. *Journal of Computational Physics*, *62*(1), 40–65. https://doi.org/10.1016/0021-9991(86)90099-9

Jasak, H., Jemcov, A., & Tukovic, Z. (2007). Openfoam: A C++ library for complex physics simulations. In *International Workshop on Coupled Methods in Numerical Dynamics* (Vol. 1000, pp. 1–20). Inter-University Centre Dubrovnik.

Kerger, F., Archambeau, P., Erpicum, S., Dewals, B. J., & Pirotton, M. (2011). A fast universal solver for 1d continuous and discontinuous steady flows in rivers and pipes. *International Journal for Numerical Methods in Fluids*, *66*(1), 38–48. https://doi.org/10.1002/fld.v66.1

Khani, D., Lim, Y. H., & Malekpour, A. (2021). A mixed flow analysis of sewer pipes with different shapes using a non-oscillatory two-component pressure approach (tpa). *Modelling*, *2*(4), 467–481. https://doi.org/10.3390/modelling2040025

Kramer, M., & Chanson, H. (2018, May). Free-surface instabilities in high-velocity air-water flows down stepped chutes. In *Proc., 7th IAHR International Symposium on Hydraulic Structures* (pp. 15–18). International Association for Hydro-Environment Engineering and Research.

Leon, A. S., Elayeb, I. S., & Tang, Y. (2019). An experimental study on violent geysers in vertical pipes. *Journal of Hydraulic Research*, *57*(3), 283–294. https://doi.org/10.1080/00221686.2018.1494052

Leon, A. S., Ghidaoui, M. S., Schmidt, A. R., & García, M. H. (2006). Godunov-type solutions for transient flows in sewers. *Journal of Hydraulic Engineering*, *132*(8), 800–813. https://doi.org/10.1061/(ASCE)0733-9429(2006)132:8(800)

Leon, A. S., Ghidaoui, M. S., Schmidt, A. R., & Garcia, M. H. (2009). Application of godunov-type schemes to transient mixed flows. *Journal of Hydraulic Research*, *47*(2), 147–156. https://doi.org/10.3826/jhr.2009.3157

Leon, A. S., Ghidaoui, M. S., Schmidt, A. R., & Garcia, M. H. (2010). A robust two-equation model for transient-mixed flows. *Journal of Hydraulic Research*, *48*(1), 44–56. https://doi.org/10.1080/00221680903565911

LeVeque, R. J., *Finite volume methods for hyperbolic problems*, Cambridge texts in applied mathematics. Cambridge University Press, 2002.

Macpherson, G. B., Nordin, N., & Weller, H. G. (2009). Particle tracking in unstructured, arbitrary polyhedral meshes for use in cfd and molecular dynamics. *Communications in Numerical Methods in Engineering*, *25*(3), 263–273. https://doi.org/10.1002/cnm.v25:3

Malekpour, A., & Karney, B. W. (2016). Spurious numerical oscillations in the preissmann slot method: Origin and suppression. *Journal of Hydraulic Engineering*, *142*(3), Article 04015060. https://doi.org/10.1061/(ASCE)HY.1943-7900.0001106

Mao, Z., Guan, G., & Yang, Z. (2020). Suppress numerical oscillations in transient mixed flow simulations with a modified hll solver. *Water*, *12*(5), 1245. https://doi.org/10.3390/w12051245

Matveev, K. I. (2020). Numerical simulation of air cavity under a simplified model-scale hull form. *Journal of Ocean Engineering and Science*, *5*(1), 68–72. https://doi.org/10.1016/j.joes.2019.08.003

Mandair, S., Magnan, R., Morissette, J.-F., & Karney, B. (2020). Energy-based evaluation of 1D unsteady friction models for classic laminar water hammer with comparison to CFD. *Journal of Hydraulic Engineering*, *146*(3), Article 04019072. https://doi.org/10.1061/(ASCE)HY.1943-7900.0001697

Moody, L. F. (1947). An approximate formula for pipe friction factors. *Transactions of ASME*, *69*(12), 1005–1011.

Murillo, J., & García-Navarro, P. (2012). Augmented versions of the hll and hllc riemann solvers including source terms in one and two dimensions for shallow flow applications. *Journal of Computational Physics*, *231*(20), 6861–6906. https://doi.org/10.1016/j.jcp.2012.06.031

Sanders, B. F., & Bradford, S. F. (2011). Network implementation of the two-component pressure approach for transient flow in storm sewers. *Journal of Hydraulic Engineering*, *137*(2), 158–172. https://doi.org/10.1061/(ASCE)HY.1943-7900.0000293

Toro, E. F. (2001). *Shock-Capturing methods for free- surface shallow flows*. Wiley and Sons Ltd.

Tosan, I., Perez-Pulido, R.-Y., Rokhzadi, A., & Fuamba, M. (2022). Additional friction factor optimized for modeling transient flows following air-pocket entrapment in stormwater systems. *Journal of Irrigation and Drainage Engineering*, *148*(2), Article 04021068. https://doi.org/10.1061/(ASCE)IR.1943-4774.0001642

USBR (1997). *Water measurement manual*. U. S. Department of the Interior, Bureau of Reclamation (USBR), U.S. Government Printing Office, 20402.

Vasconcelos, J. G., Wright, S. J., & Roe, P. L. (2006). Improved simulation of flow regime transition in sewers: Two-component pressure approach. *Journal of Hydraulic Engineering*, *132*(6), 553–562. https://doi.org/10.1061/(ASCE)0733-9429(2006)132:6(553)

Vasconcelos, J. G., Wright, S. J., & Roe, P. L. (2009). Numerical oscillations in pipe-filling bore predictions by shock-capturing models. *Journal of Hydraulic Engineering*, *135*(4), 296–305. https://doi.org/10.1061/(ASCE)0733-9429(2009)135:4(296)

Weller, H., Tabor, G., Jasak, H., & Fureby, C. (1998). A tensorial approach to computational continuum mechanics using object orientated techniques. *Computers in Physics*, *12*, 620–631. https://doi.org/10.1063/1.168744

Zhou, L., Alain, E., & Karney, B. (2019). Unsteady friction in a rapid filling pipeline with trapped air. In *Proc., 38th IAHR World Congress* (09, pp. 3386–3393). International Association for Hydro-Environment Engineering and Research.